An experimental investigation into the effect of Cu_2O particle size on antifouling roughness and hydrodynamic characteristics by using a turbulent flow channel

Chang Li[a], Mehmet Atlar[b], Maryam Haroutunian[a], Colin Anderson[c], Serkan Turkmen[a]

[a] Newcastle University, UK
[b] University of Strathclyde, Glasgow, UK.
[c] American Chemet Corporation, USA

Corresponding author: Maryam Haroutunian
E-mail: maryam.haroutunian@newcastle.ac.uk; Telephone: 0191 20 86104

Abstract

Copper and copper compounds are commonly used as biocides against biofouling on surfaces exposed to seawater. Copper oxide, one of the most commonly used forms of copper biocide, can provide an efficient mechanism for fouling-free surfaces, resulting in substantial fuel savings and reduction of Greenhouse Gases (GHG) emissions. However, copper oxide is commercially formulated with different particle sizes, which can consequently lead to surfaces with different roughness conditions. The roughness effect of various sizes of copper oxide particles on the drag performance of antifouling coatings, and hence on the ship hull drag, has not been systematically studied in the past. Therefore, to investigate the effect of particle sizes on antifouling roughness and hydrodynamic characteristics, a number of different sized cuprous oxide pigments (with median size ranging from 2μm to 250μm) were applied on Newcastle University's (UNEW) standard acrylic flat test panels. Roughness characteristics were analysed by using an optical surface profilometer. Moreover, the microstructure observations of all test specimens were carried out using Scanning Electron Microscopy (SEM). Subsequently, a laboratory experiment of streamwise pressure drop measurements was conducted on all coated plates and compared to uncoated acrylic control panels. The Reynolds number for the experiment, based on bulk mean velocity and channel height, ranged from 3×10^4 to 1.6×10^5. Analysis indicated that for the panels coated with particle sizes $\geq 12\mu m$, the roughness characteristics and frictional drag increased as particle size increased. Interestingly, due to particle agglomeration and surface finish condition, those panels coated with particle sizes $< 12\mu m$ were found not follow this trend and had higher roughness and drag characteristics than expected.

Keywords

Copper oxide, antifouling, roughness characteristic, frictional drag, pressure drop measurement, roughness function

Nomenclature

h, b	Inner dimension size of the channel height and beam
B	Smooth wall log-law intercept=5.0
f	Fanning Friction Factor
C_f	Skin friction coefficient
D	Hydraulic Diameter
D_{10}	Particle diameter at 10% in the cumulative distribution.
D_{50}	Particle diameter at 50% in the cumulative distribution.
D_{90}	Particle diameter at 90% in the cumulative distribution
D_Z	The number of zero crossing with the mean line
g	Gravitational acceleration
H	Channel height
k	Roughness length scale
k^+	Roughness Reynolds number
ΔP	Pressure drop values
Re_D	Reynolds number based on duct hydraulic diameter
R_a	Arithmetic average height

R_q	Root Mean Square (RMS) Roughness height
R_t	Peak to trough roughness height
R_{sk}	Skewness
R_{ku}	Kurtosis
S_m	Defined as the mean spacing between profile peaks at the mean line, measured over the assessment length.
$\bar{U}$	Bulk mean velocity
ΔU^+	Roughness Function
u_τ	Friction velocity
Δ_a	Mean slope of the profile
Δx	Streamwise pressure dropping distance
λ_a	Average wavelength
κ	Von Karman constant=0.41
ν	Kinematic Viscosity
ρ	Density
τ_w	Wall shear stress

Superscript

$+$	Inner variable (normalized with U_τ or U_τ/ν)

Subscript

max	Maximum value
min	Minimum value
R	Rough surface
S	Smooth surface

1. Introduction

At present, 95% of global bulk trade involves transport by sea with significant fuel consumption and corresponding exhaust emissions. According to the reports from the Third International Maritime Organization (IMO) GHG Study (Smith *et al.*, 2014) over the period of 2007 to 2012 international shipping was estimated to have produced an average of 846 million tonnes of CO_2, which is equivalent to 2.7% of global CO_2 emissions. Smith *et al.* (2014) estimated that the annual global CO_2 emissions of 2012 were dominated by three ship types: oil tankers (124 million tonnes), bulk carriers (166 million tonnes) and container ships (205 million tonnes).

Marine fouling can increase ship hull surface roughness and result in ship efficiency loss. Biofilm (slime) is the primary stage of biofouling and can be formed within hours of a ship or other marine structures being immersed in seawater (Candries *et al.*, 2003a). Biofilm is believed to cause frictional drag increase of up to 10% on full-scale ships (Watanabe *et al.* (1969). Controlling biofouling by applying antifouling (AF) paints can reduce the frictional drag and subsequently the fuel consumption as well as the GHG emissions. In a most recent investigation on the effect of biofilms on ship hull resistance Yeginbayeva (2017) presented perhaps the most comprehensive and systematic study exploring the effect of slime on Foul-Release (FR) type coating performance by using naturally and dynamically grown biofilms in the sea environment, as well as artificially cultivated slime in a laboratory environment. This study also recommended a procedure to estimate the effect of biofilm on ship hull resistance based on Granville's procedure (Granville, 1987) by using the experimentally determined database for roughness functions of surfaces with biofilms.

Copper and copper compounds have been used since the 16th century as effective antifouling agents. As an AF biocide, copper is known to protect marine immersed surfaces from tube worms, barnacles and most types of algal fouling. For those ship hull surfaces protected with inorganic copper compounds (such as Cu_2O, CuO, Cu_2S, and CuS), copper is released into the water in the form of copper ions Cu^{2+} or Cu^{+}. Under natural conditions, Cu^{+} ions will be oxidised immediately into Cu^{2+} ions, their main biocidal form, which is more stable (Zhao and Wang, 2015).

As AF coatings are commonly used for preventing fouling settlement on ships' hulls, much attention has been paid to evaluating and estimating their antifouling performance and drag penalties, either using experimental models or from results of full-scale ships coated with AF coatings. Research interests have investigated the effects of copper-based AF coatings on surface roughness and drag penalties. Haslbeck and Bohlander (1992) and Holm *et al.* (2004) performed drag measurements on copper-component ablative AF coatings by using rotating disk apparatus, but without surface roughness evaluations at each experimental stage and fouling condition. Especially for an ablative coating matrix, it would be expected that the surface roughness changes while it is reacting with seawater, and therefore the roughness needs to be observed during the tests. Candries *et al.* (2003b) used rotating disk drag tests to study Foul-Release (FR) and Self Polishing Co-polymer (copper SPC) AF coatings. Two cylinders were coated with an FR scheme and a copper SPC scheme respectively, by spray application; one other cylinder was coated with an FR scheme by roller application. It was noted that the finished surfaces were expected to be rougher when the coating was applied by a roller in comparison to spray application. It was concluded that roughness comparisons under the same coating application methods are required for more accurate roughness estimation.

Towing tank measurements were carried out on flat plates allowing for the comparison of the frictional drag of Tin-free AF with that from FR coatings (Candries, 2001; Candries *et al.*, 2003a; Schultz, 2004). It was found that SPC copper had the highest roughness amplitudes and frictional force, followed by the ablative copper scheme, whilst the FR scheme exhibited the lowest roughness amplitude and frictional force. The results are in agreement with the work of Candries *et al.* (2003b), who found the roughness amplitudes and frictional resistance of SPC copper to be higher than that of the FR scheme under the same application procedure. Also, the SPC copper scheme was found to have a higher frictional resistance than the FR scheme according to water tunnel tests carried out by Candries and Atlar (2005).

For any processed surface, understanding the impact of natural irregular particles on coating microstructure and surface roughness is essential. One of the main issues stems from the fact that it is harder to evaluate a three-dimensional irregular shaped particle, for example a sand grain or a pigment, with a unique number (Rawle, 2002). As a result, a body of research focuses on the interaction of surface roughness and particle size due to coating properties, addressing questions such as how particle size can affect viscosity, dispersion stability and surface roughness. Heslin *et al.* (1974) studied the surface roughness effect of different sized glass-sphere particles. Particle sizes of 10 to 40 and 40 to 80 microns were tested, and it was established that roughness increases with particle size. However, the limitation of the study is that only artificial regular shaped particles were tested instead of irregularly shaped particles. Kong *et al.* (2007) carried out studies of average powder effect on surface roughness and powder deposition efficiency. Five groups of different sized Inconel 625 Nickel alloy, ranging from 37µm to 158µm, were tested. The study found that the highest powder deposition efficiency did not result from the largest or the smallest particle size powder. Both large and very small particles were associated with high roughness with evident waviness. However, for minuscule particles, only coagulation within the nozzle was discussed by Kong *et al.* (2007). A discussion from Rawle (2002) indicated that the phenomena of agglomeration and aggregation could occur for very small particles which may cause suspension during the particle powder application. Further research focusing on particles from different materials of the same size ranges is lacking.

Moreover, the interaction between surface roughness and particle size may also be affected by other factors. Irzaman *et al.* (2011) investigated surface roughness and grain size under annealing temperature effects. They found that with temperature increasing, the RMS roughness and grain size decreased, which showed a strong correlation with annealing temperature. Xin *et al.* (2010) studied thickness dependence of particle size and surface roughness. Furthermore, there is evidence that thickness increases with grain size, which causes higher surface roughness (Melo *et al.* (2004); Xin *et al.* (2010)). An investigation of surface roughness with Nano-crystalline Aluminium was conducted by (Perron *et al.*, 2008) using mean grain sizes of 5, 10, 15 and 20 nm. They respectively evaluated the surface roughness changes from elastic and plastic deformations. Roughness insignificantly increased during the elastic deformation, however they found it changed rapidly in the plastic domain. This research studied temperature, layer thickness and deformation aspects of nanometre-scale particles, but the results for larger scale grain sizes are not very clear.

Based on the literature review it was established that there is a gap in the existing literature on AF coatings performance from different sizes of cuprous oxide particles. Surface roughness characteristics and frictional drag performance have not been systemically studied. The focus of this paper is to investigate surface roughness effects of different sizes of cuprous oxide particles on the drag performance of antifouling coatings by using an experimental pressure drop method. To achieve this aim the paper has been organised as follows: in Section 2 the background of pressure drop testing and roughness function evaluation methodology are presented. The introduction to the experimental setup and a wall function formulation for current test is proposed in Section 3.

In Section 4, uncertainty analyses for the pressure drop test and roughness function are included. Analysis and discussion of SEM images and roughness statistical results, along with frictional coefficient and roughness function, are presented in Section 5. Finally, a set of conclusions obtained from the study is included in Section 6.

2. Pressure Drop Testing and Roughness Function

Rough pipe turbulent flow has been studied by many outstanding researchers including (Darcy, 1857), (Bazin, 1902), (Stanton, 1911), (von Mises, 1914), (Schiller, 1923), (Hopf, 1923) in the past centuries. Continuing those previous investigations, Nikuradse (1933) conducted experiments of pressure drop measurements in rough pipes coated with artificial uniform sand, for investigating the effect of various degrees of relative roughness on turbulent flow. From Nikuradse's experimental observations, the flow conditions can be divided into three ranges, following the law of resistance in each range. Colebrook and White (1937), Colebrook *et al.* (1939) and Moody (1944) have extended Nikuradse's work. Colebrook and White (1937) indicated that there was a gradual transition between the smooth and rough resistance laws. The work of Colebrook *et al.* (1939) presented the analysis of commercial pipes that was based on the previous observations that transition from smooth-law to rough-law takes place in a gradual manner.

Moody (1944) attempted to estimate the friction factor in head loss in clean new pipes with steady flow. As one of the most common fluid engineering tools, Moody diagram curves are based on the Colebrook function (Colebrook *et al.*, 1939). It relates pressure drop with relative pipe roughness (ratio of the roughness height to the pipe hydraulic diameter). In line with Nikuradse (1933)'s resistance law ranges, the Moody diagram represents three flow regimes: (1) the hydraulically smooth regime, where the projections of roughness lie entirely within laminar layer, and roughness effects are a function of Reynolds number; (2) the transitionally rough regime, where wall shear stress increases, caused by projections of roughness from the laminar layer, therefore roughness effects are a function of both Reynolds number and roughness characteristics; (3) the fully rough regime, where all projections of roughness extend through the laminar layer, and roughness effects are independent of Reynolds number but are still a function of roughness characteristics.

For general surface roughness cases, however, there are some limitations regarding application of the Moody diagram. The roughness length scale, k_s used in the Moody diagram, is called the equivalent sand-grain roughness height. For a surface, the k_s is experimentally determined instead of the actual roughness height. The accurate results of a surface could be demonstrated by the Moody diagram only when the certain value of k_s has been obtained, but this is still unknown for most other surfaces (Flack and Schultz, 2010). Some experiments showed that in the transitionally rough regime of the Moody diagram, surfaces did not follow the Colebrook function (Schultz and Flack, 2007). Allen *et al.* (2005) evaluated a universal transitional resistance diagram for honed finish pipes and they found inflectional behaviour in the transitionally rough regime.

In order to precisely describe the roughness effects on skin friction in a range of pipe roughness, a parameter of roughness function, ΔU^+ was introduced. Surface roughness would not only increase the drag penalty and resulting heat transfer but would also affect the near wall mean velocity profile. By following the classical log-law, the mean velocity profile of the inner region of the smooth wall turbulent boundary layer can be given as follows:

$$U^+ = \frac{1}{\kappa}\ln(y^+) + B \qquad \text{Eq. 1}$$

where κ is the von Karman constant and B is the intercept for a smooth wall

The parameter of roughness function, ΔU^+, presents a downward shift on the mean velocity log-law profile comparing the rough-wall to the smooth-wall under the primary effect of roughness (Hama, 1954) and (Clauser, 1954). Therefore the log-law for rough and smooth walls can be written as:

$$U^+ = \frac{1}{\kappa}\ln(y^+) + B - \Delta U^+ \qquad \text{Eq. 2}$$

As proposed by Hama (1954), the roughness function, ΔU^+ can be expressed as the difference in skin frictional coefficient, C_f, from smooth wall to rough wall at the same displacement thickness Reynolds number, Re_{δ^*}, as below:

$$\Delta U^+ = \left(\frac{2}{C_f}\right)^{1/2}_{smooth} - \left(\frac{2}{C_f}\right)^{1/2}_{rough} \quad \text{Eq. 3}$$

The roughness function, ΔU^+ for pressure drop measurement of the turbulent channel were found by similarity law analysis of Granville (1987). For fully developed channel pipe flow, the roughness function is determined at the given Reynolds number:

$$\Delta U^+ = \left(\frac{2}{f}\right)^{1/2}_{smooth} - \left(\frac{2}{f}\right)^{1/2}_{rough} \quad \text{Eq. 4}$$

where f is defined as fanning friction factor:

$$f = 2\left(\frac{u_\tau}{\overline{U}}\right)^2 \quad \text{Eq. 5}$$

It is noted that the skin friction data from the rough and the smooth surfaces are compared at equal values of $Re_D\sqrt{f}$.

As provided by Granville the relationship between the roughness function and frictional drag has been instrumental in extrapolating the skin friction of various rough surfaces to full-scale, based on the experimentally derived roughness functions and boundary layer wall-similarity method. For example, the drag of larger planer surfaces polished by wet sanding can be predicted (Schultz, 2002) based on the experimentally predicted roughness functions using the Granville similarity law (Granville, 1978). Following the same similarity law procedure, Schultz (2007) also estimated the powering penalties of ship hulls due to different types of antifouling and different grades of marine fouling. On regular geometries surface distributions, studies of suitable roughness length scales for close-packed pyramid surfaces were reported by Schultz and Flack (2009). Within a similar context, numerous researchers have conducted investigations on the roughness length scales of different types and applications of coatings in Newcastle University. Candries (2001) gave the roughness function and roughness length scales studies on FR and tin-free SPC coatings under their different application schemes through towing tank measurements. Other roughness function studies of foul release coatings were carried out by Ünal (2012) and Ünal *et al.* (2012) using zero-pressure-gradient boundary layer tests. Nevertheless, those research works (Candries (2001); Ünal (2012); Ünal *et al.* (2012)) were all concentrated mainly on the FR type coating. In a recent investigation, Ünal (2015) suggested a new definition for the roughness length scale considering the effects of the roughness calculation methods and difference application procedures of other antifouling coatings. In the most recent study conducted in Newcastle, Yeginbayeva (2017) presented the roughness length scales for not only cleanly applied different types of commercial FR coatings but also for these surfaces under the effect of biofilm.

3. Experimental Facilities and Methods

For investigating the effects of surface roughness characteristics of various sized particles, eight different sizes of particles of Cu_2O were produced by American Chemet Corporation. Table 1 describes Cu_2O particle diameter at 10% (D_{10}), 50% (D_{50}) and 90% (D_{90}) in the cumulative distribution, along with Cu_2O particle weight content (%) of each type of powder. In this paper, these cuprous oxide particles are named hereafter as C2, C7, C12, C17, C25, C60, C100 and C250 where "n" in Cn stands for the rounded-up value of the corresponding D_{50} in the cumulative distribution.

From these a coating was formulated with 75% of cuprous oxide particles and 25% of VC17M Extra-Part B as binder. The AF coatings were applied on Newcastle University's (UNEW) standard acrylic flat testing panels with air-assisted spray application. The VC17M Extra-Part B uses a volatile solvent as a carrier, therefore the finished dry film (20~150μm in thickness) consisted mainly of cuprous oxide particles, >90% by weight. The strength and insolubility of the matrix enabled the AF coating to be tested under high water flow Reynolds number. Furthermore, as the dry AF coating contained over 90% cuprous oxide, it can be considered as a hypothetical surface of pure cuprous oxide (Carlton, 1998). It should be noted that these coatings were purely experimental, and not at all similar to commercially available antifoulings. Commercial antifoulings generally have a cuprous oxide content of < 50% (dry film weight), and are applied by airless spray at film thicknesses well in excess of 100 microns.

Table 1: Statistical description of Cu_2O powder

Powder	D_{10} (μm)	D_{50} (μm)	D_{90} (μm)	Cu_2O (%)
C2	0.7	1.4	2.5	>95
C7	4	7	12	>95
C12	5	12	23	>95

C17	10	17	25	>95
C25	11	25	57	>95
C60	32	61	89	>95
C100	40	97	170	>95
C250	190	246	366	>95

The pressure drop measurements were performed in the turbulent flow channel, which was designed and recently further enhanced in the testing section, (Turkmen *et al.*, 2016), at the School of Marine Science and Technology, Newcastle University, United Kingdom, as shown in Figure 1. The test section of the channel is 10 mm in height (H), 180 mm in width (W), and 2.7 m in length (L). Dean (1978) postulated the minimum aspect ratio 7:1 to ensure two-dimensional flow in the turbulent channel. Monty (2005), Schultz and Flack (2013) both have approved Dean's conclusion of an aspect ratio (W/H) of 18:1 to be more than sufficient to provide two-dimensional flow along the centreline of the channel.

The discharge tank of the facility can hold 6000 L of water, and the temperature of the water was controlled constantly at 20 ± 0.25 ℃ via a cooling coil fitted in the discharge tank linked to a refrigeration unit. The flow is produced by a max of 15kW centrifugal pump which can provide flow rates up to 300L/s and it is computer controlled by separate variable frequency drive units. The pumps operate in parallel and generate a bulk mean velocity of $1.62 - 8.30\ \mathrm{ms}^{-1}$ in the test section. The resulting Reynolds number (Re_D) based on the duct hydraulic diameter and bulk mean velocity ranges from 3×10^4 to 1.6×10^5.

A stainless honeycomb flow straightener with 5 mm diameter cells, and 100 mm in length is fitted in the settling chamber upstream of the test section. The flow is tripped at the entrance through a two-dimensional nozzle with contraction ratio of 34.7:1. According to Durst *et al.* (1998) and Schultz *et al.* (2000), for obtaining a fully-developed turbulent channel at Reynolds numbers $> 3 \times 10^3$, a slot for fitting UNEW's standard test panel ($L \times W = 598mm \times 218mm$) is opened at ~192H downstream to the channel inlet. This allows two identical test panels to be placed at the top and bottom of the pressured drop test section to form the top and bottom boundary of the test section.

Along one of the side walls of the test section, there are nine pressure taps located at 164H–262H downstream of the trip at the inlet to the channel. These are 0.75 mm holes located along the centreline of the side wall of the test section. Two XMD Process Plant DP cell differential pressure transmitters are installed for measuring the pressure differences. Their measuring ranges are up to 75 and 500 mbar respectively with the accuracy of ±0.1% of the full scale. A side LDA glass windows (with a cross-section of $10 \times 150\mathrm{mm}$) is installed between pressure taps 7 and 8 to allows optical access to the channel.

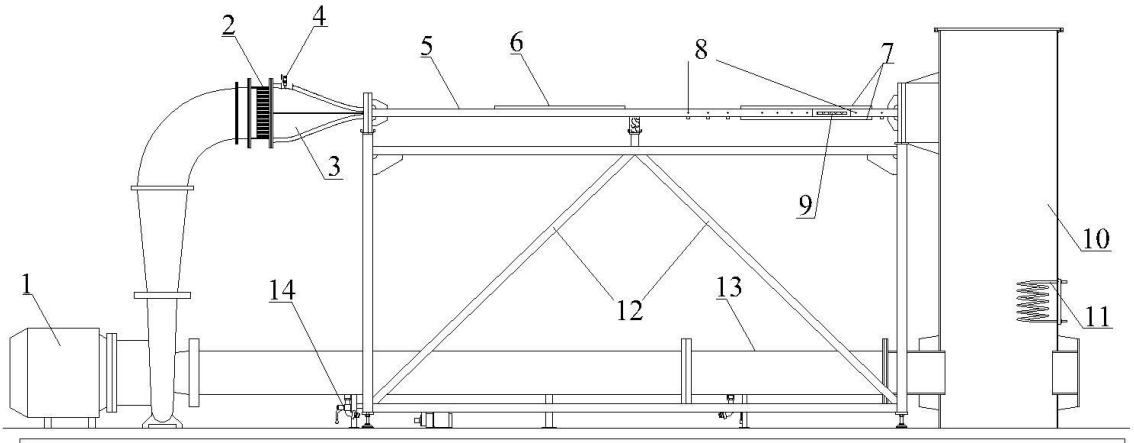

1. Centrifugal Pump	6. Inspection Test Plate	11. Cooling Coil
2. Honeycomb	7. Test Plates	12. Support Construction
3. Contraction	8. Pressure Taps	13. Duct
4. Ball Valve	9. LED Window	14. Draining Valve
5. Measuring Test Section	10. Reservoir	

Figure 1: Side view of turbulent flow channel integral structure

For the present investigation, four pressure taps from No.5 (x = 209H) to No.8 (x = 249H) were used for measuring the pressure drop from the test surfaces. Seven bulk velocities of 1.62ms^{-1}, 2.87ms^{-1}, 4.1ms^{-1}, 5.17ms^{-1}, 6.29ms^{-1}, 7.45ms^{-1}and 8.30ms^{-1}were applied with five pressure dropping distances of 0.075m, 0.15m, 0.25, 0.325m and 0.4m. The pressure drop data were collected at a sample rate of 10Hz for a sampling period of 100s until 10,000 data were obtained at each pressure dropping distance per each bulk mean velocity.

The skin-friction coefficient, C_f is typically expressed as:

$$C_f = \left(\frac{\tau_w}{0.5\rho\bar{U}^2}\right) = 2\left(\frac{u_\tau}{\bar{U}}\right)^2 \quad \text{Eq. 6}$$

By combining Eq. 5 and Eq. 6, we have:

$$C_f = 2\left(\frac{u_\tau}{\bar{U}}\right)^2 = f \quad \text{Eq. 7}$$

The wall shear stress, τ_w, was determined by streamwise pressure drop values, dp at each pressure dropping distance, dx. It is calculated as follows:

$$\tau_w = -\frac{D}{2}\frac{dp}{dx} \quad \text{Eq. 8}$$

$$u_\tau = \left(\frac{\tau_w}{\rho}\right)^{\frac{1}{2}} \quad \text{Eq. 9}$$

where D is the hydraulic diameter, p is the static pressure value, x is the streamwise pressure dropping distance, ρ is the fluid density, $\bar{U}$ is the bulk mean velocity, u_τ is the frictional velocity and water density ρ is taken as 998 kg/m^3 (at the temperature 20°C). For non-circular flow channel, the hydraulic diameter, D is commonly calculated as follows:

$$D = \frac{4hb}{2(h+b)} = \frac{2hb}{h+b} \quad \text{Eq. 10}$$

where h and b are the dimensions of the inner height and beam of the channel respectively. The Reynolds number based on the hydraulic diameter, and bulk mean velocity, $\bar{U}$ (or mean velocity) can be expressed as:

$$Re_D = \frac{D\bar{U}}{\nu} \quad \text{Eq. 11}$$

where ν is the kinematic viscosity of the fluid.

As noted by Zanoun et al. (2009) there is no significant variation in the streamwise pressure drop for x ≥ 20H. This was supported by observations from Schultz and Flack (2013) whose pressure drop values were constantly within experimental uncertainty from the first pressure tap located at x = 63H. In the present experiment, the pressure drop measurements were constantly taken downstream of the pressure tap No.5 (x = 209H) with an experimental uncertainty ≤ 0.3% at the lowest bulk mean velocity to ≤0.09% at the highest bulk mean velocity.

The surface roughness of the test surfaces was measured using an OSP100A non-contact roughness profilometer. The optical laser sensor was adjusted on the two-axis traverse with positioning range of 90mm × 60mm (x × y). 120 linear profiles were measured at a scanning speed of 25mm/s. The statistical analysis of surface roughness were calculated using the Gaussian filter with a 2.5mm cut-off length which is a commonly used value (Standard ISO 4287, 1997). In this paper roughness statistics were demonstrated by five roughness amplitude parameters: arithmetic mean height (R_a), root-mean-square deviation (R_q), total height (R_t), skewness (R_{sk}), kurtosis (R_{ku}), and two spacing texture parameters: mean slope of the profile, (Δ_a) and average wavelength, (λ_a). The formulae for these seven roughness parameters are as follows:

$$R_a = \frac{1}{n}\sum_{i=1}^{n}|y_i| \quad \text{Eq. 12}$$

$$R_q = \sqrt{\frac{1}{n}\sum_{i=1}^{n}|y_i{}^2|} \quad \text{Eq. 13}$$

$$R_t = \overset{max}{i} y_i - \overset{min}{i} y_i \quad \text{Eq. 14}$$

$$R_{sk} = \frac{1}{nR_q^3}\sum_{i=1}^{n} y_i^3 \quad \text{Eq. 15}$$

$$R_{ku} = \frac{1}{nR_q^4}\sum_{i=1}^{n} y_i^4 \quad \text{Eq. 16}$$

$$\Delta_a = \frac{1}{\mathrm{n}-1}\sum_{\mathrm{i}=1}^{n-1}\left(\frac{\delta_{y_i}}{\delta_{x_i}}\right) \quad \text{Eq. 17}$$

$$\lambda_a = \frac{2\pi R_a}{\Delta_a} \quad \text{Eq. 18}$$

where y_i is the vertical distance from the mean line to its profile and n is the number of the points on each profile.

4. Uncertainty Estimates

In this work, for the uncertainty analysis of the roughness measurements, the 95% precision confidence limits for a given quantity were obtained by multiplying its standard error by the two-tailed t value (t=1.96) for the number of degrees of freedom over 120 (Coleman and Steele Jr, 1990). To calculate the uncertainty of the tests for frictional drag measurement, the pressure drop tests made with each pair of identical test panels were repeated five times based on the Moffat (1988) method. The 95% precision confidence limits for a given quantity were obtained by multiplying its standard error by the two-tailed t value (t=2.776) for four degrees of freedom (Coleman and Steele Jr, 1990).

As explained in Section 5 below, two sets of experiments were carried out. For the 1st set of pressure drop tests, the resulting precision and bias uncertainties in the skin-friction coefficient, C_f, ranged from ±3.2% to ±9.2% at the lowest Reynolds number for each test, to ±0.8% to ±1.5% at the highest Reynolds number for each test. As for the 2nd set of tests, the resulting precision and bias uncertainties in C_f ranged from ±2.1% to ±5.1% at the lowest Reynolds number for each test, to ±0.18% to ±1.9% at the highest Reynolds number at each test. The overall precision and bias error for roughness function, ΔU^+ of the 1st experiment ranged from ±3.3% to ±17.0% at the lowest Reynolds number, to ±0.5% to ±3.4% at highest Reynolds number. The overall precision and bias error for roughness function, ΔU^+ of the 2nd experiment ranged from ±4.0% to ±15.4% at the lowest Reynolds number, to ±0.6% to ±3.2% at highest Reynolds number.

5. Results and Discussion

The presentation of the results and discussion is arranged as follows: first, the microstructure observations of the test specimens are demonstrated by SEM images analysis. Next, the discussion of statistical results from each test surface is made. It has to be noted that microstructure analysis and roughness measurements were applied on small microscopy slides and test panels separately. After this, the results from pressure drop measurements are presented and discussed. Finally, a roughness function, ΔU^+, is proposed for all the tested surfaces.

A second set of experiments were also carried out due to the unusual roughness and friction drag characteristics of the small size specimens (i.e. specimen C2 and C7) that were measured in the first set of experiments. The coatings from the first experiments were removed from the test surfaces and then re-coated with the same size specimens, minimising as much as possible the external interfering factors such as human error, the powder application device and the environment (mainly humidity).

The impacts from the different particle sizes were systematically studied by comparing the results from the two sets of experiments. It has to be noted that two images are shown for special cases, C2 and C7 in Figures 2 (see Figures 2 (a), (b), (c) and (d)) and Figure 3 (see Figure 3 (a), (b), (c) and (d)), due to their notable surface differences in the two sets of applications.

5.1 Roughness Analysis

The microstructure of the test surfaces was evaluated using SEM. Figures 2 gives SEM views for surfaces coated with tested specimens (i.e. C2−C250) along with their magnification ratio (i.e. *650×, 200× and 100×*). In the case of C2, Figures 2(a) shows a critical rough surface with significant "clumping" and wider interspaces between particles in the 1st application compared to the 2nd application (Figures 2 (b)). For the case of C7, the 2nd application condition (Figures 2(d)) compared to the 1st application (Figures 2(c)) shows a slightly higher particle density and smaller spaces between particles. As particles size increases (Figures 2(e), 2(f), 2(g), 2(h), 2(i) and 2(j)) the full contact between particles turns into a partial contact. As a result, wider and deeper gaps are formed.

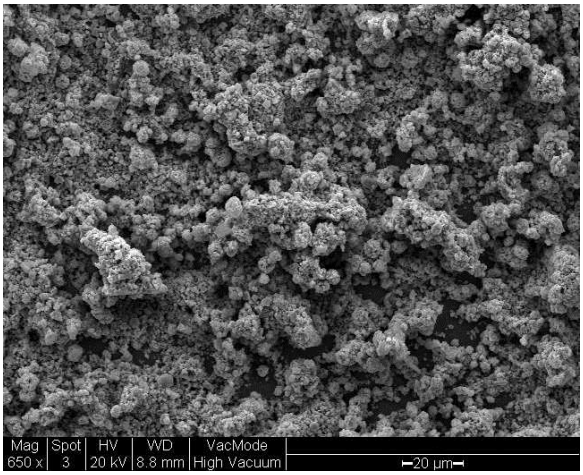

*(**a**). Surface covered with C2 in the 1st application (650× magnification)*

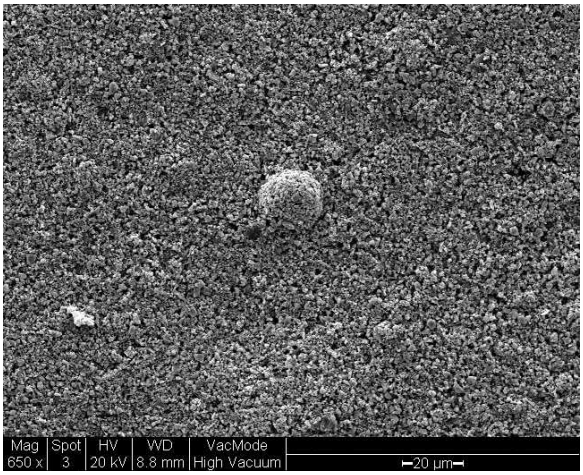

*(**b**). Surface covered with C2 in the 2nd application (650× magnification)*

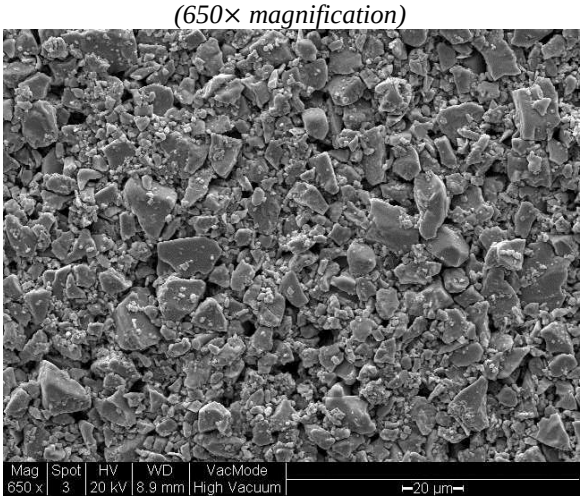

*(**c**). Surface covered with C7 in the 1st application (650× magnification)*

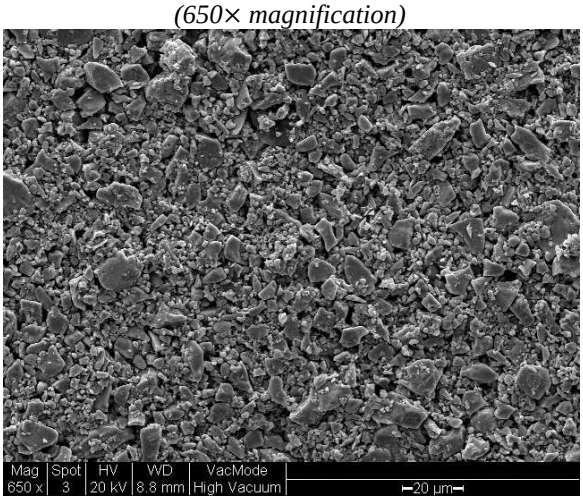

*(**d**). Surface covered with C7 in the 2nd application (650× magnification)*

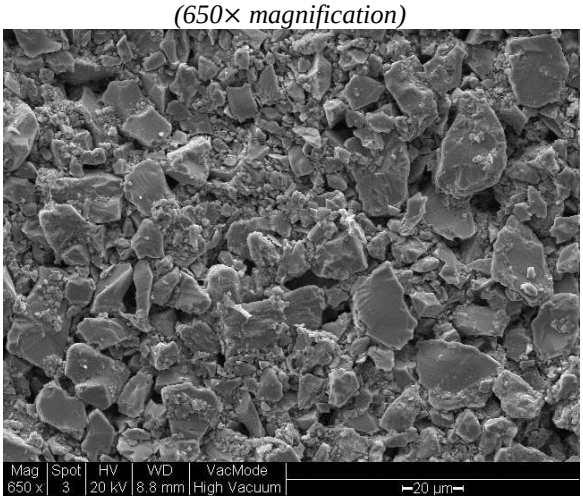

*(**e**). Surface covered with C12 (650× magnification)*

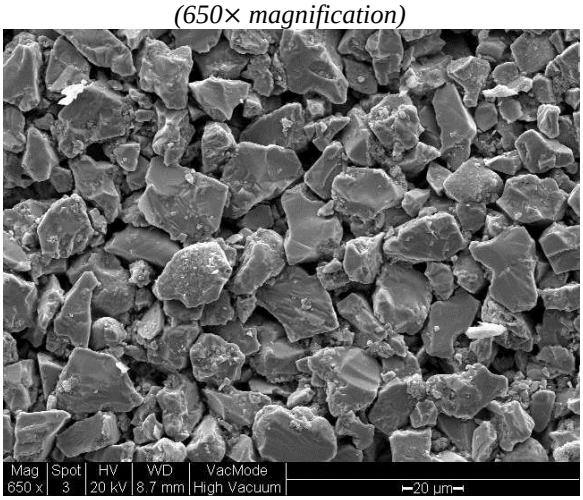

*(**f**). Surface covered with C17 (650× magnification)*

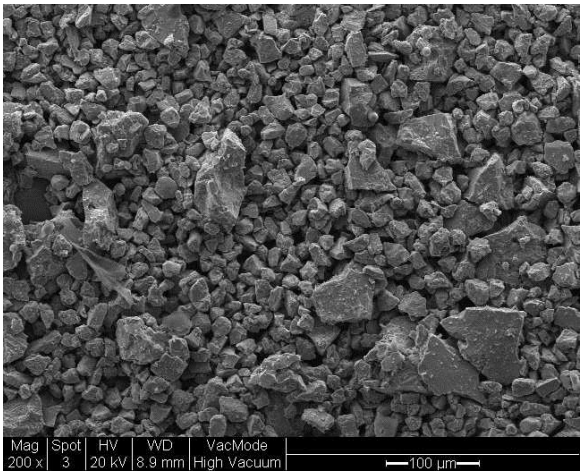

*(**g**). Surface covered with C25 (200× magnification)*

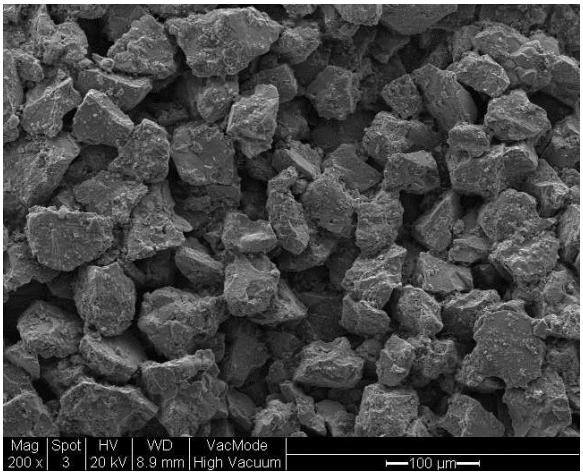

*(**h**). Surface covered with C60 (200× magnification)*

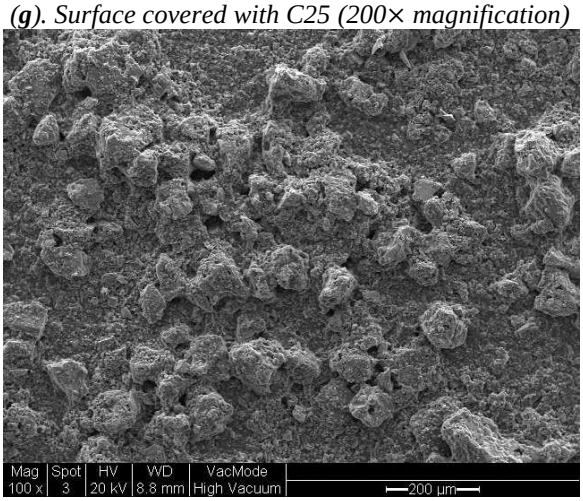

*(**i**). Surface covered with C100 (100× magnification)*

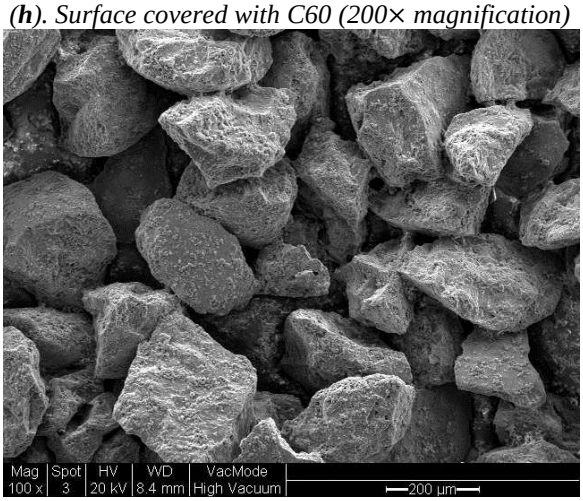

*(**j**). Surface covered with C250 (100× magnification)*

Figures 2: (a) − (j). SEM top-view of the test surfaces coated with cuprous oxide particle specimens

The cross-section of these specimens and their magnification ratios (i.e. *1500×, 800×, 650×, 350× and 150×*) are presented in Figure 3. Figure 3 (a) shows that the 1st application of C2 had a "coral" shape structure which dramatically increased the surface waviness profile. Figure 3 (b) shows C2 from the 2nd application with increased layer thickness and a smoother top surface profile. However self-aggregated materials with loose internal structures can be clearly observed. Surfaces with C7 have a low surface waviness profile. Compared with Figure 3 (c), Figure 3 (d) shows C7 had a thicker layer of coating and carried a higher density of particles in the 2nd application. This leads to particles packing more adequately and hence less interspaces were present. As particle size increases, (Figure 3 (e), (f), (g), (h), (i) and (j)) surfaces are getting rougher due to the microstructures consisting of larger size specimens, with wider spacing gaps between particles.

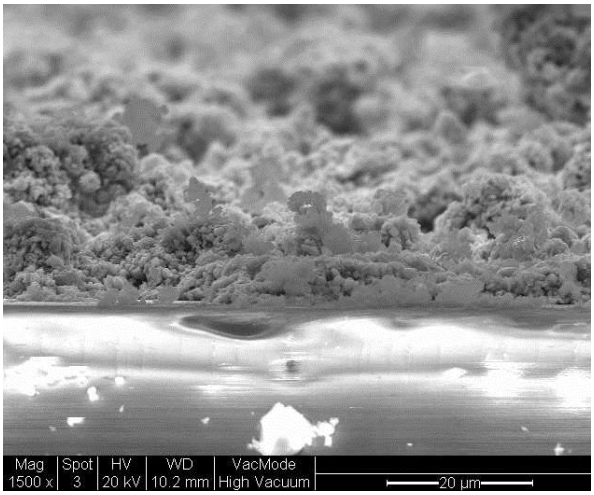

***(a)**. Cross-section of C2 from the 1st application (1500× magnification)*

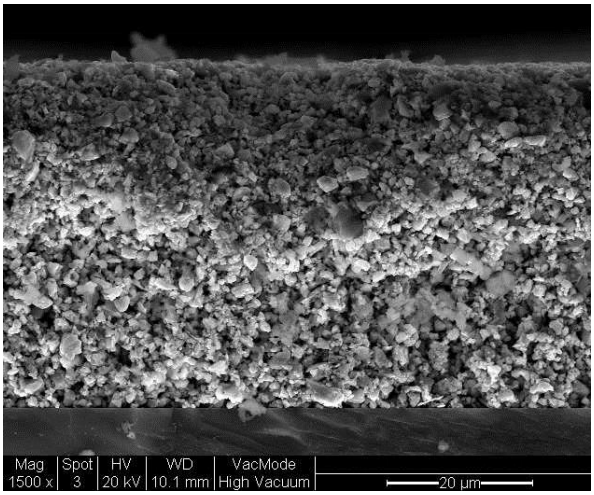

***(b)**. Cross-section of C2 from the 2nd application (1500× magnification)*

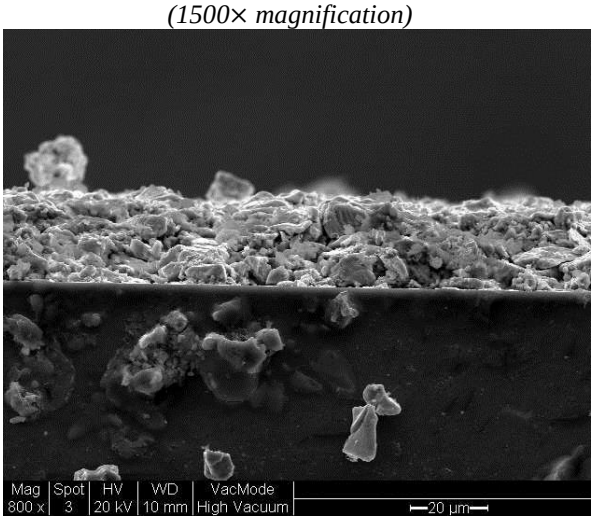

***(c)**. Cross-section of C7 from the 1st application (800× magnification)*

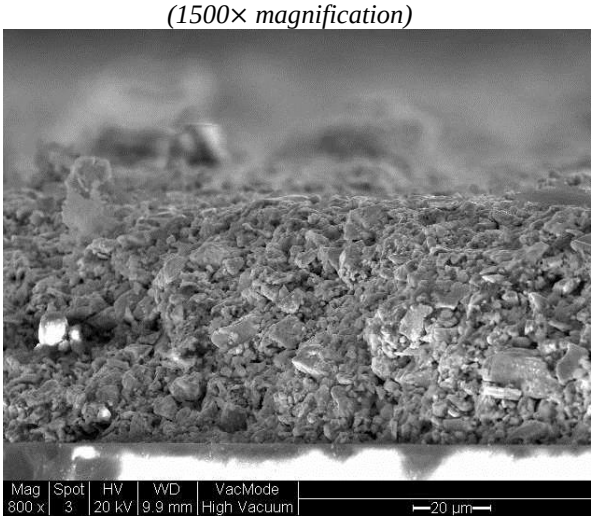

***(d)**. Cross-section of C7 from the 2nd application (800× magnification)*

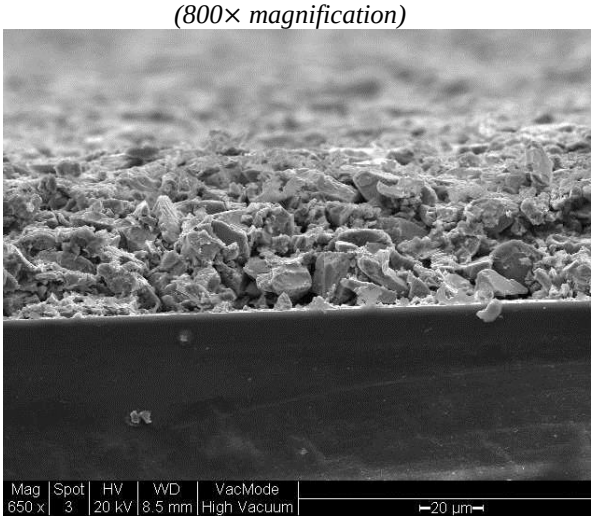

***(e)**. Cross-section of C12 (650× magnification)*

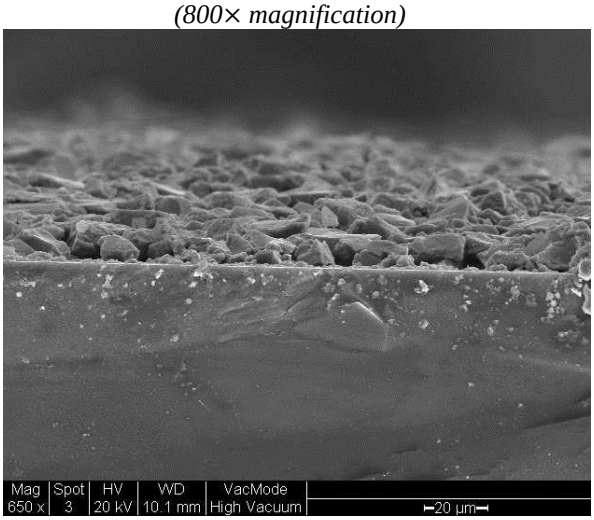

***(f)**. Cross-section of C17 (650× magnification)*

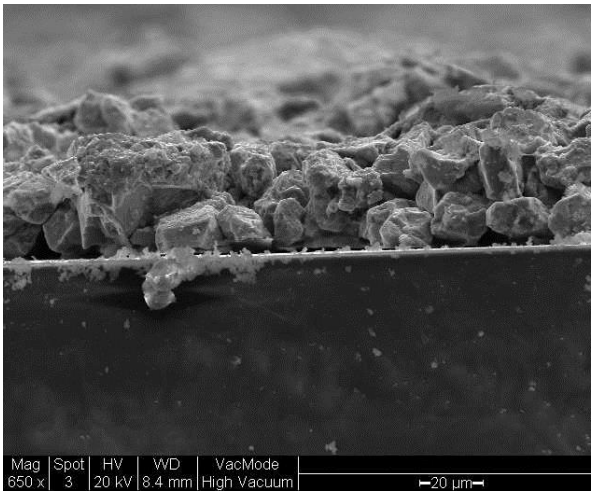

*(**g**). Cross-section of C25 (650× magnification)*

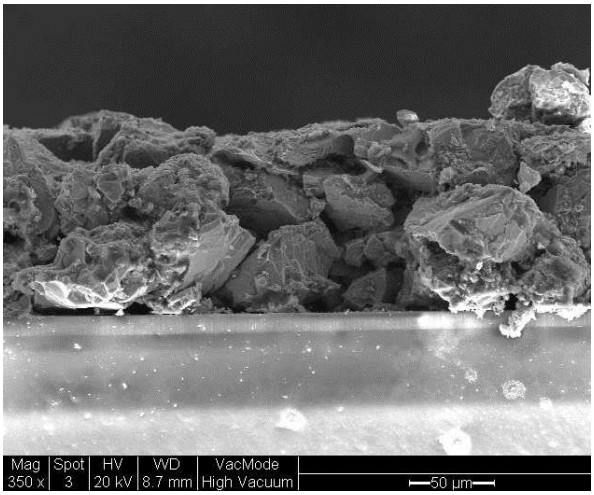

*(**h**). Cross-section of C60 (350× magnification)*

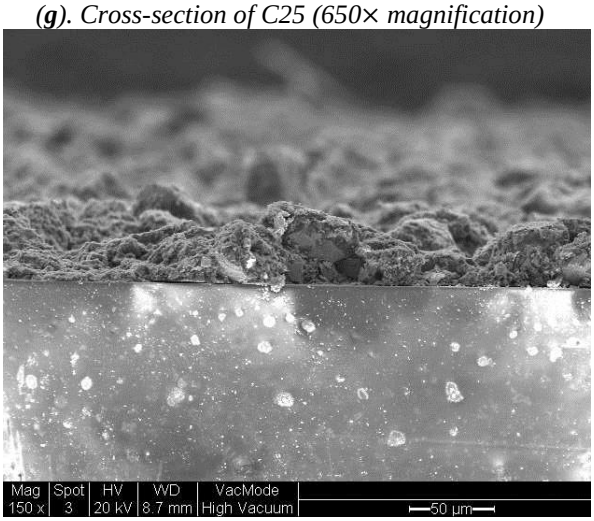

*(**i**). Cross-section of C100 (150× magnification)*

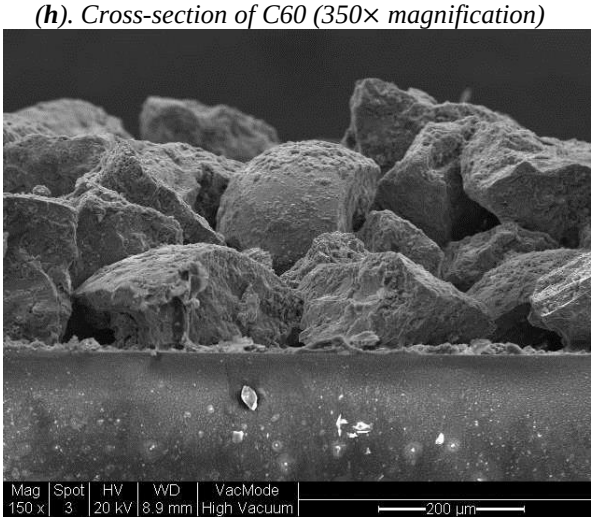

*(**j**). Cross-section of C250 (150× magnification)*

Figure 3: (a−j). SEM cross-sections of test surfaces covered with cuprous oxide particles

Table 2 shows the analysis results of roughness statistics for all the test surfaces under the above-described conditions. To form a closed channel, two identical coated panels are installed on the top and bottom of the test section slots. In order to distinguish the roughness statistics from each panel, the top and bottom panels are marked as "A" and "B", respectively. Surface topography maps have been provided in Appendix A, which show further details about the surface conditions. The analysis of roughness parameters for all tested particles indicated that, except for C2 and C7, amplitude parameters (R_a, R_q, R_t and R_Z) are directly related to the particle size. For C12, C17, C25 and C60 specimens, roughness amplitude increases gradually with an increase in partial size. For particle sizes $D_{50} > 60\mu m$ (i.e. C100 and C250), the roughness parameters dramatically increased. Comparing the roughness values between both applications, it can also be seen that it was only in the case of the second application of C60 where there was a significant difference, with the roughness increased to roughly twice that from first application. In the cases of C2 and C7, even though these specimens are marked as very small sized particles in the present investigation, the roughness amplitudes from these specimens are greater than those for four of the other tested specimens (i.e. C12, C17, C25 and C60).

Table 2: Roughness Statistics (uncertainty represent the 95% confidence precision bounds for the measurements)

Specimen	Test Series	Surface	R_a (µm)	R_q (µm)	R_t (µm)	R_{sk}	R_{ku}	Δ_a	λ_a (µm)
C2	Test_1	A	9.3±0.2	12.8±0.4	68.1±2.0	0.047±0.005	4.9±0.1	0.089±0.001	630.0±7.7
		B	5.3±0.1	7.3±0.2	39.4±1.3	0.046±0.009	5.1±0.2	0.055±0.000	587.1±8.6
	Test_2	A	8.4±0.2	12.4±0.4	68.2±2.2	0.071±0.006	6.1±0.2	0.085±0.001	592.3±8.9
		B	11.4±0.4	16.1±0.6	80.5±2.9	0.041±0.005	4.9±0.1	0.087±0.001	759.6±12.7

C7	Test_1	A	11.0±0.2	13.6±0.2	61.3±1.0	-0.017±0.002	3.0±0.1	0.078±0.000	875.7±8.1
		B	10.7±0.1	14.8±0.2	76.9±0.9	0.118±0.002	6.0±0.1	0.174±0.001	447.3±7.9
	Test_2	A	2.6±0.0	3.3±0.0	18.5±0.3	-0.049±0.009	3.5±0.1	0.055±0.000	297.0±2.8
		B	2.1±0.0	2.7±0.1	15.9±0.4	-0.022±0.010	3.7±0.1	0.051±0.000	260.1±2.6
C12	Test_1	A	2.4±0.0	3.0±0.0	17.7±0.2	0.022±0.007	3.7±0.1	0.052±0.000	275.8±2.1
		B	2.2±0.0	2.9±0.0	16.7±0.3	0.032±0.007	3.5±0.1	0.056±0.000	252.8±2.4
	Test_2	A	2.4±0.0	3.1±0.1	17.4±0.3	0.028±0.008	3.5±0.1	0.055±0.000	273.6±2.3
		B	2.6±0.0	3.3±0.1	18.5±0.3	0.003±0.009	3.5±0.1	0.057±0.000	284.8±3.3
C17	Test_1	A	2.8±0.0	3.5±0.0	20.0±0.2	0.031±0.006	3.5±0.1	0.064±0.000	264.1±3.6
		B	4.9±0.1	6.4±0.2	34.1±0.9	0.072±0.005	3.9±0.1	0.079±0.000	378.7±5.3
	Test_2	A	3.0±0.0	3.8±0.0	20.6±0.3	0.020±0.006	3.2±0.1	0.063±0.000	294.7±2.2
		B	2.8±0.0	3.5±0.0	19.4±0.3	0.031±0.006	3.3±0.1	0.063±0.000	273.1±1.8
C25	Test_1	A	4.8±0.0	6.1±0.0	32.8±0.3	0.003±0.003	3.3±0.1	0.085±0.000	330.1±2.0
		B	4.6±0.0	5.8±0.0	31.6±0.2	0.009±0.004	3.3±0.0	0.092±0.000	315.3±3.4
	Test_2	A	4.1±0.0	5.2±0.1	28.4±0.4	-0.033±0.006	3.5±0.1	0.078±0.000	326.2±2.6
		B	4.1±0.0	5.2±0.1	28.2±0.4	-0.013±0.006	3.4±0.1	0.078±0.000	327.0±2.5
C60	Test_1	A	6.6±0.1	8.3±0.1	43.7±0.4	0.018±0.003	3.3±0.1	0.097±0.000	427.3±4.5
		B	6.8±0.1	8.7±0.1	47.6±0.5	-0.037±0.003	3.6±0.1	0.121±0.000	364.0±3.8
	Test_2	A	14.6±0.2	18.1±0.2	88.2±0.9	-0.001±0.001	2.8±0.0	0.211±0.001	438.5±4.0
		B	16.1±0.2	19.9±0.2	95.6±1.0	0.001±0.001	2.7±0.0	0.216±0.001	471.3±4.4
C100	Test_1	A	20.7±0.2	26.8±0.3	131.4±1.8	0.052±0.001	4.9±0.1	0.264±0.001	492.5±3.4
		B	18.4±0.1	22.8±0.2	112.7±1.0	0.006±0.001	2.9±0.0	0.247±0.001	468.8±3.3
	Test_2	A	19.0±0.2	23.6±0.2	117.4±1.1	0.001±0.001	2.8±0.0	0.303±0.001	397.8±2.5
		B	19.5±0.2	24.2±0.2	121.6±1.3	-0.007±0.001	2.9±0.0	0.307±0.001	400.3±2.8
C250	Test_1	A	66.5±0.5	83.0±0.6	394.1±3.2	-0.001±0.000	2.9±0.0	0.631±0.002	673.6±8.2
		B	45.8±0.4	58.0±0.4	281.7±2.2	-0.003±0.000	3.1±0.0	0.436±0.002	679.5±8.6
	Test_2	A	65.1±0.7	77.3±0.7	307.5±2.6	0.003±0.000	2.4±0.0	0.461±0.002	902.6±9.2
		B	69.9±0.8	83.9±0.9	341.3±3.6	0.003±0.000	2.5±0.0	0.495±0.003	903.1±9.9

It is worth noting here that particle coagulation was observed with C2 and C7, which tended to block the spray nozzle and jam the chamber of the spray gun. According to the air-assisted spray principle, particles can be delivered only under sufficient air pressure. The very minuscule particles, mixed with larger coagulated particles, were pushed out inconsistently and this resulted in pulsed spraying, giving uneven surface textures. As a consequence, additional surface roughness was built up. It was observed however that specimen C7 can be better dispersed into the binder, without agglomeration. As a result, an improved surface for C7 in the 2nd application was achieved, with the lowest roughness characteristic. As indicated in the case of C7, surface roughness is affected by both microstructure roughness and macrostructure roughness, with the latter dominating.

5.2 Frictional Resistance

Shown for smooth surface comparison, an empirical power relation proposed by Dean (1978) and Zanoun *et al.* (2009) is given in Eq. 19 and Eq. 20 respectively:

$$C_f = 0.073Re^{-0.25} \quad \text{Eq. 19}$$

for the Reynolds number range: $6 \times 10^3 < Re < 6 \times 10^5$.

$$C_f = 0.0743Re^{-0.25} \quad \text{Eq. 20}$$

The un-coated cast acrylic panels were used to represent smooth surfaces. Skin friction coefficients from eight specimens as well as the smooth surfaces, measured via each pressure drop test, are plotted in Figure 4 (first set of pressure drop tests) and Figure 5 (second set of pressure drop tests).

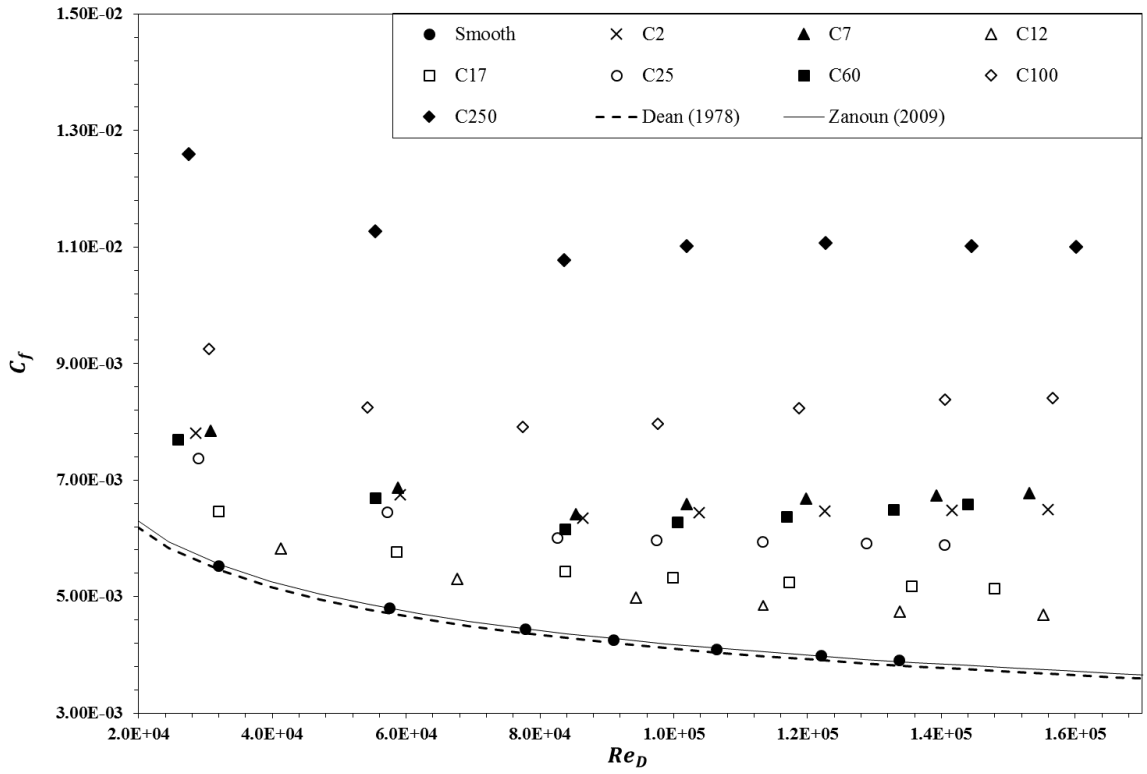

Figure 4: Frictional coefficient results for the first pressure drop test. (Overall uncertainty in C_f: ±3.2% to ±9.2% at the lowest Reynolds number, ±0.8% to ±1.5% at the highest Reynolds number)

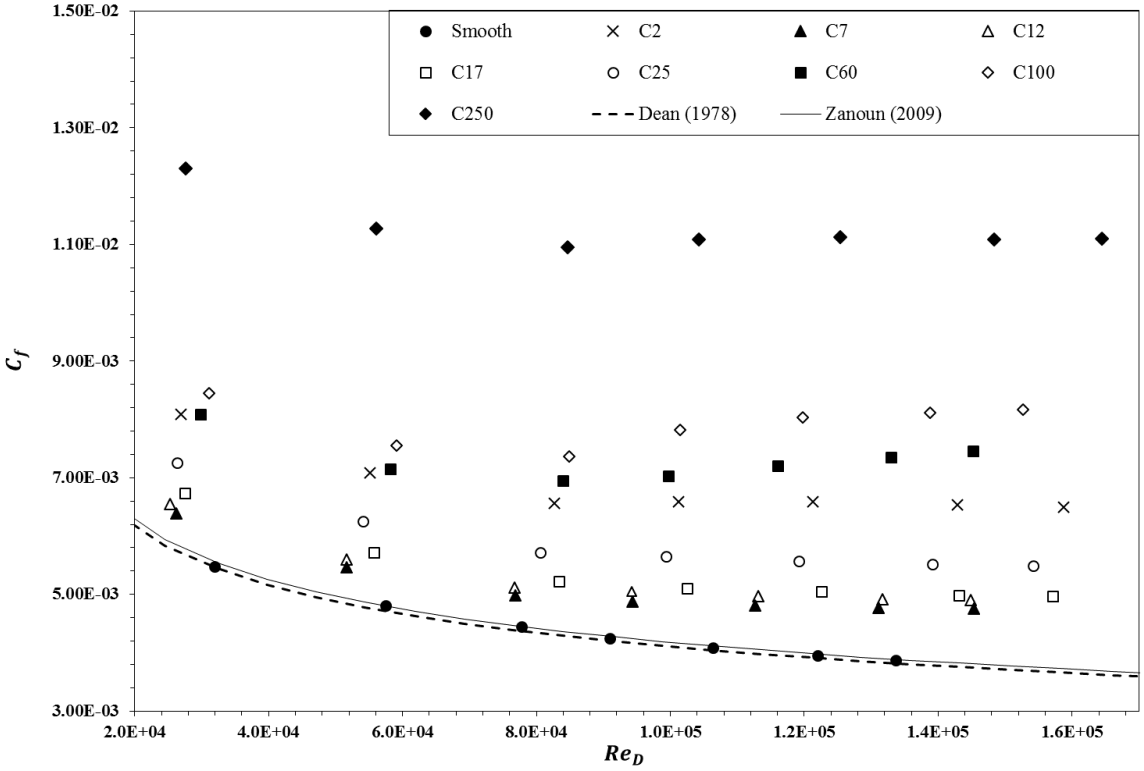

Figure 5: Frictional coefficient results for the second pressure drop test. (Overall uncertainty in C_f: ±2.1% to ±5.1% at the lowest Reynolds number, ±0.18% to ±1.9% at the highest Reynolds number)

The present smooth surface results show agreement with the mean line of Dean (1978) and Zanoun *et al.* (2009) over the entire Reynolds number range. Apparent inflectional behaviour occurred on some tested specimens in the transitional regime. According to the discussion of Allen *et al.* (2005), inflectional behaviour can be observed in the transitional regime, when the relative surface roughness $R_q/D < 2.5 \times 10^{-3}$. In this research, due to the closed channel, an average value of relative surface roughness from each pair of panels (top and bottom) has been taken into account. The relative surface roughness values of all specimens is tabulated in Table 3.

Table 3: relative surface roughness for the test specimens

First experiment								
Specimens	C2	C7	C12	C17	C25	C60	C100	C250
R_q/D	5.3×10^{-4}	7.5×10^{-4}	1.6×10^{-4}	2.6×10^{-4}	3.1×10^{-4}	4.5×10^{-4}	1.3×10^{-3}	3.7×10^{-3}
Second experiment								
Specimens	C2	C7	C12	C17	C25	C60	C100	C250
R_q/D	7.5×10^{-4}	1.6×10^{-4}	1.7×10^{-4}	1.9×10^{-4}	2.7×10^{-4}	1.0×10^{-3}	1.3×10^{-3}	4.3×10^{-3}

For the two sets of experiments, within the Reynolds number range, the C_f curves of C12 and C17 kept a trend similar to the smooth surface. An inflectional behaviour in which the friction coefficient curve slightly turns-upward at $Re_D > 8 \times 10^4$ were observed for all specimen except C12 and C17. During the 2nd experiment, due to the relative surface roughness decrease, no inflectional behaviour was observed in specimen C7 and the C_f curve has the same trend as C12. The inflectional behaviour is dependent on both Reynolds number and the roughness characteristics (Nikuradse, 1933). In addition, results of the very large specimen (C250) from both experiments show a mild inflectional behaviour, which diminishes at high Reynolds numbers where the curve becomes parallel to the horizontal axis. This shows that the roughness effects are independent of the Reynolds number at higher Reynolds numbers ($Re_D > 1 \times 10^5$)

To provide further insight into the friction drag vs. different surface roughness condition with their cuprous oxide specimens, Table 4 shows the increase (%) in friction coefficient for the test surfaces compared to the smooth surface. Among all eight tested specimens, except for the very small specimens (i.e. C2 and C7), results from both the 1st and 2nd experiments indicated that frictional coefficient increased from that of the smooth surface with the increase in particle size, from between approximately 10% to 160%. For the 1st experiment, the lowest drag was demonstrated by specimen C12 (14%) and this was followed by C17 (25%). For those very small size particles, on average, specimen C2 had about 52% increase in C_f, with C7 56%. In the 2nd experiment, the specimen C7 resulted in a much lower C_f value, only 17%, which is imperceptibly lower than those of C12 (20%) and C17 (23%). Specimen C2 In the 2nd experiment still resulted in considerably high values of C_f for its particle size (an average 56% increase). From both 1st and 2nd experiments, the highest average friction was approximately 157% and this was obtained from C250. Then this is followed by C100 (86%) and C60 (59%). Based on the experiments presented here, it can be noted that the relative higher C_f values of specimen C2 and the dramatic difference between the two C7 tests are dependent on their surface macro finish quality.

Table 4: Increase in overall C_f for the test specimens compared to the cast acrylic surface

Specimen	**Test No.**	**R_t (μm)average**	**Average Increase in C_f (%)**	**Range of Increase in C_f (%)**
C2	1	53.7	51.7	40.5−66.3
	2	74.4	56.0	47.3−67.7
C7	1	69.1	55.6	41.9−73.5
	2	17.2	16.9	12.1−22.7
C12	1	17.2	13.5	5.4−19.8
	2	18.0	20.4	15.1−26.7
C17	1	27.1	24.9	17.0−31.5
	2	20.0	22.5	17.4−28.1
C25	1	32.2	41.0	33.4−50.9
	2	28.3	34.6	28.7−41.9
C60	1	45.6	50.3	38.7−68.7

	2	91.9	67.6	47.4−92.4
C100	1	122.0	90.0	67.2−115.2
	2	119.5	82.0	54.1−110.8
C250	1	337.9	155.9	127.9−181.6
	2	324.4	158.0	124.3−186.5

5.3 Roughness Function

For a roughness function plot, ΔU^+ vs. k^+, the non-dimensional roughness height, k^+, which represents the roughness Reynolds number, is determined as:

$$k^+ = \frac{k u_\tau}{\nu} \qquad \text{Eq. 21}$$

where k is the roughness length scale and ν/u_τ is the viscous length scale. Figure 6 and Figure 7 illustrate the relationship between average roughness function, ΔU^+, and roughness height, k^+, of surfaces for each test. Nikuradse type roughness function and Colebrook type roughness function values are also presented for comparison. Nikuradse (1933) roughness function based on uniform sandgrain results was proposed by Ligrani and Moffat (1986) as:

$$\Delta U^+ = \left(\frac{1}{\kappa}\ln + \mathrm{C} - 8.5\right)\sin\left(\frac{\pi g}{2}\right)$$
$$g = \frac{lnk_s^+ - lnk_S^+}{lnk_R^+ - lnk_S^+} \quad k_S^+ < k_s^+ < k_R^+ \qquad \text{Eq. 22}$$
$$g = 1 \quad k_R^+ < k_s^+$$
$$g = 0 \quad k_s^+ < k_S^+$$

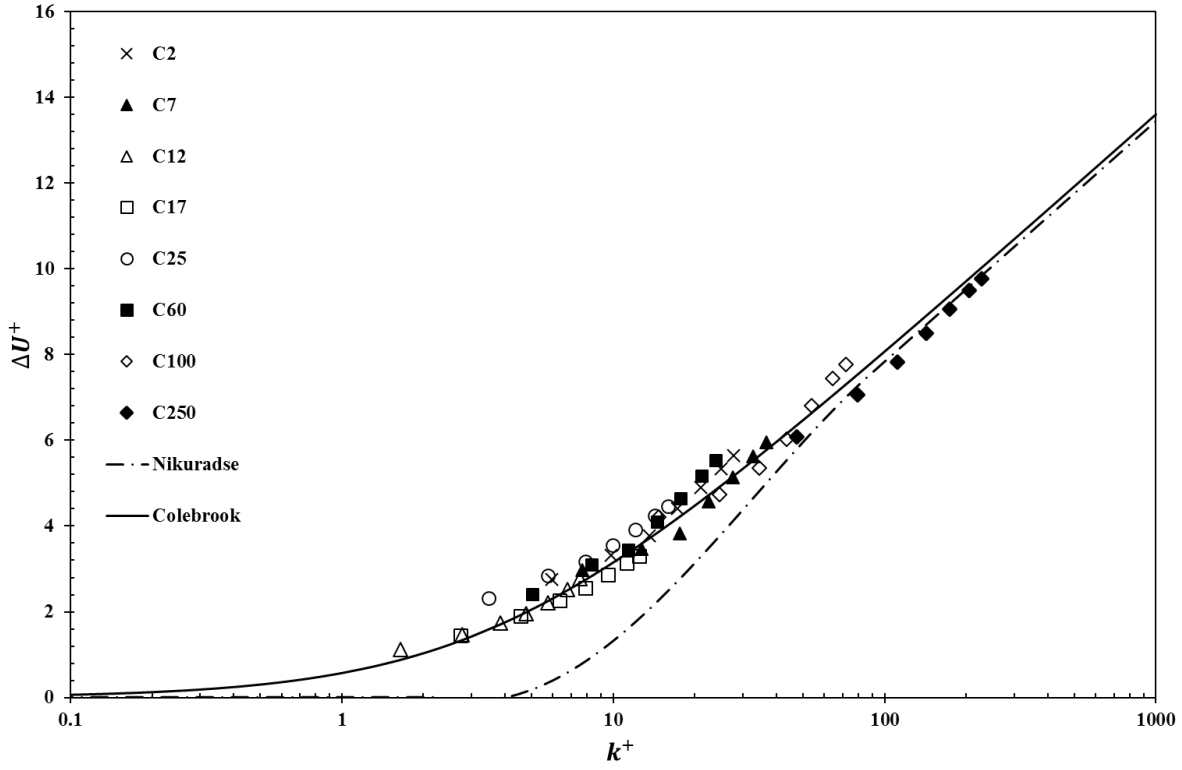

Figure 6: Roughness function results for the first pressure drop test scaled on $k = 1.1R_t$. (Overall uncertainty in ΔU^+: ±3.3% to ±17.0% at the lowest Reynolds number, ±0.5% to ±3.4% at the highest Reynolds number)

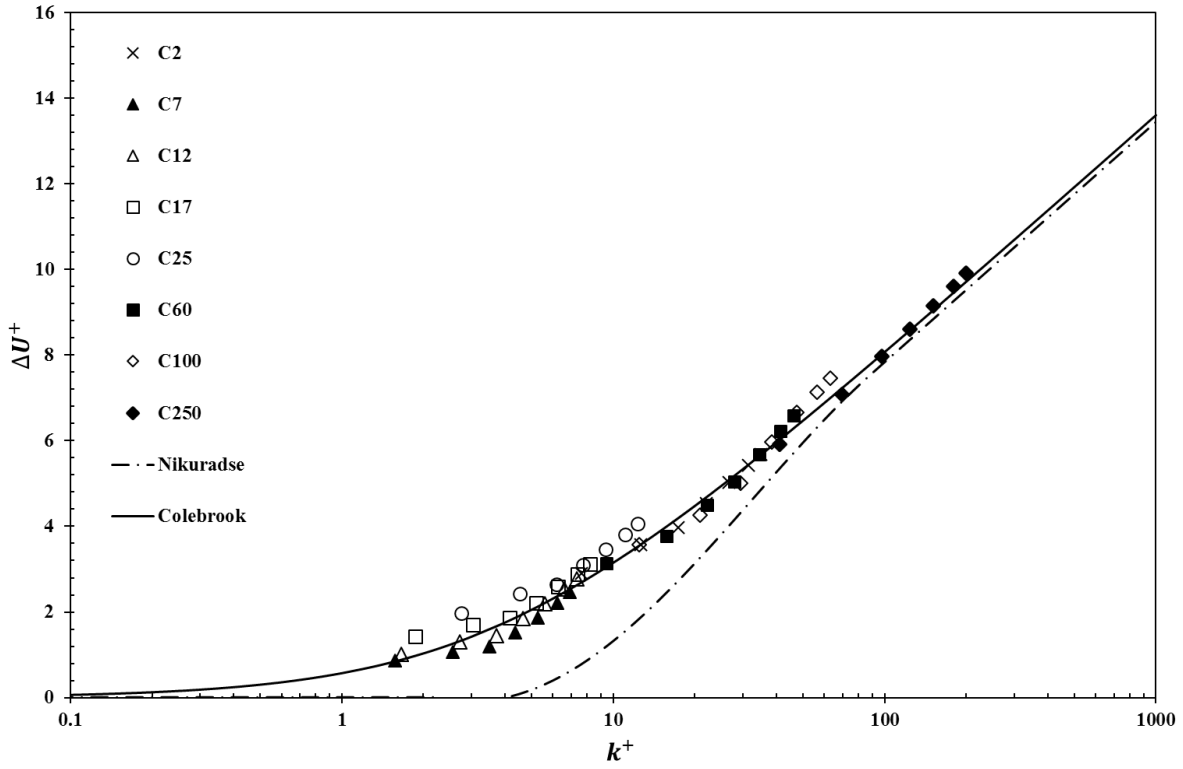

Figure 7: Roughness function results for the second pressure drop test scaled on $k = R_t$. (Overall uncertainty in ΔU^+: ±4.0% to ±15.4% at the lowest Reynolds number, ±0.6% to ±3.2% at the highest Reynolds number)

The Colebrook-White function was developed for engineering surfaces. The Colebrook type roughness function (Colebrook et al., 1939) is given by Aupoix (2015) as shown in Eq.22:

$$\Delta U^+ = \frac{1}{\kappa}\ln(1 + \frac{k^+}{exp[\kappa(8.5 - C)]}) \quad \text{Eq. 23}$$

where the von Karman constant, κ, is equal to 0.41. The intercept constant, C is 5.25 for Colebrook type roughness function and 5.1 for Nikuradse type roughness function. The lower critical roughness Reynolds number is $k_S^+ = 2.25$ and upper critical roughness Reynolds number is $k_R^+ = 90$.

It has to be noted that the choice of a roughness length scale only affects the abscissa of roughness function profiles along with the roughness Reynolds number, without affecting roughness function values. For selecting a suitable roughness length scale, several options have been considered. For example, a multiple of the centreline average roughness height, R_a (with model $k = AR_a$, where A is an arbitrary constant) (Schultz, 2002), or a multiple of the peak to trough roughness height, R_t (with model $k = AR_t$) (Schultz, 2004; Flack *et al.*, 2012). In addition, some research work has proposed the application of combined roughness parameters to calculate the roughness length scale. For example, Candries (2001) used the mean slope of the profile, Δ_a, multiplied with centreline average roughness height, R_a ($k = \Delta_a R_a/2$). Moreover, a combination of root-mean-square, R_q, and skewness, R_{sk} (with model $k = AR_q(1 + R_{sk})^B$) was proposed by Flack and Schultz (2010) and later modified by Ünal (2015) who introduced the mean spacing between the zero-crossings, Sd_4, and therefore $k = AR_q(1 + R_{sk})^B/Sd_4$.

In this paper, a multiple of the peak to trough roughness height, $k = AR_t$ was obtained as the best roughness length scale to fit to Eq.22. Regression analysis indicated that, respectively for the first and second test, with $k = 1.1R_t$ and $k = R_t$ the resulting values showed a reasonable agreement with the Colebrook type roughness function behaviour in the transitional rough regime. 97.5% (i.e. $R^2 = 0.975$) and 97.1% (i.e. $R^2 = 0.971$) of the variance in the first and second test results can be explained by Colebrook type roughness function respectively. The results of roughness function along with the associated k^+ are presented in Table 5. Based on observations from the SEM images, even though these tested surfaces were like "micro-scale sandpaper", roughness function results obviously did not exhibit uniform sandgrain results of Nikuradse type roughness function behaviour in the transitionally rough regime.

Table 5: The results of roughness function ΔU^+ along with the associated k^+ values

First experiment															
C2		***C7***		***C12***		***C17***		***C25***		***C60***		***C100***		***C250***	
k^+	ΔU^+	k^+	ΔU^+	k^+	ΔU^+	k^+	ΔU^+	k^+	ΔU^+	k^+	ΔU^+	k^+	ΔU^+	k^+	ΔU^+
6.0	2.8	7.7	3.0	1.6	1.1	2.7	1.4	3.5	2.3	5.0	2.4	14.7	4.2	47.6	6.1
9.8	3.3	12.7	3.5	2.8	1.5	4.6	1.9	5.7	2.8	8.3	3.1	24.6	4.7	79.8	7.1
13.6	3.8	17.6	3.8	3.9	1.7	6.3	2.3	7.9	3.2	11.4	3.4	34.5	5.4	111.4	7.8
17.3	4.4	22.5	4.6	4.8	1.9	7.9	2.6	9.9	3.6	14.5	4.1	43.6	6.0	142.0	8.5
21.0	4.9	27.5	5.1	5.8	2.2	9.6	2.9	12.1	3.9	17.8	4.7	53.9	6.8	173.3	9.1
25.0	5.3	32.7	5.6	6.8	2.5	11.2	3.1	14.3	4.2	21.2	5.2	64.5	7.4	204.7	9.5
27.8	5.6	36.6	6.0	7.6	2.8	12.5	3.3	15.9	4.5	23.8	5.5	71.9	7.8	227.9	9.8
Second experiment															
C2		***C7***		***C12***		***C17***		***C25***		***C60***		***C100***		***C250***	
k^+	ΔU^+	k^+	ΔU^+	k^+	ΔU^+	k^+	ΔU^+	k^+	ΔU^+	k^+	ΔU^+	k^+	ΔU^+	k^+	ΔU^+
7.6	2.9	1.6	0.9	1.7	1.0	1.9	1.4	2.8	2.0	9.4	3.1	12.5	3.6	41.0	5.9
12.7	3.6	2.6	1.1	2.7	1.3	3.1	1.7	4.5	2.4	15.7	3.8	20.9	4.3	69.6	7.1
17.4	4.0	3.5	1.2	3.7	1.4	4.2	1.9	6.2	2.7	22.1	4.5	29.5	5.0	98.0	8.0
22.0	4.5	4.4	1.5	4.6	1.8	5.2	2.2	7.7	3.1	28.0	5.1	38.4	6.0	124.3	8.6
26.7	5.0	5.3	1.9	5.6	2.2	6.3	2.6	9.4	3.5	34.5	5.7	47.3	6.7	151.5	9.2
31.5	5.4	6.2	2.2	6.6	2.5	7.4	2.9	11.0	3.8	41.3	6.2	56.3	7.1	179.1	9.6
35.0	5.7	6.9	2.5	7.4	2.8	8.2	3.1	12.3	4.1	46.4	6.6	63.0	7.5	199.7	9.9

There was no observation of k^+ value for the onset of the transitional rough regime, whereas the fully rough regime started at the roughness Reynolds number, $k^+ = 20$. The transitional rough regime was within $1.5 < k^+ < 20$ for the present results, where $k^+ = 1.6$ was the lowest experimental roughness Reynolds number. In the transitional rough regime, except for the C7, the lowest ΔU^+ values were obtained by C12 among all tested surfaces, and this was followed by C17 and C25. As the roughness Reynolds number increased, within the same testing speed range, flow over C2, C60 and C100 was passing from the transitional rough regime into the fully rough regime. The ΔU^+ values scattered in the fully rough regime agree with the full flow asymptotic lines of Colebrook's behaviours at $k^+ > 20$.

6. Conclusions

This paper presented a practical and efficient method to measure the skin-friction and roughness characteristics of flat surfaces covered with a cuprous oxide-based coating. The roughness characteristics measurements were carried out using an optical roughness measurement device. Furthermore, a turbulent flow channel was used to measure the pressure drop to assess the effect of roughness on the frictional drag characteristics of the test surfaces. The above mentioned methods and measurements were subsequently used to highlight optimized selection from several different sizes of Cu_2O specimens by comparing and correlating their roughness and hydrodynamic characteristics. Observations of microscale structures have clearly indicated that initial roughness of the surfaces are dependent on the particle size as well as the quality of coating application. Bad application of the coating caused by the particle agglomeration will directly affect the surface roughness. In practical terms, the smallest size specimen did not give the expected lowest roughness characteristics. As a chain reaction, the friction drag was directly affected. For the roughness function, the peak-to-trough roughness height is used as the roughness length scale. The results of the roughness function and the regression value showed good agreement with the Colebrook type roughness function. The roughness function within the fully rough regime agreed well with both the fully rough asymptotic line and the inflectional behaviour in the transitionally-rough regime. The measurements of specimens C2 and C7 showed that the quality of paint application can have a significant effect on the roughness function and associated resistance increase. Also, as the different concentrations of copper particles indicated, paint formulation and associated roughness can have a significant influence on the drag characteristics. As highlighted in Section 3, the test coatings were formulated in a laboratory environment, and do

not realistically represent commercial products. Commercial products would result in different test results. No hydraulic smooth regime was observed from the present investigation.

7. Acknowledgments

The authors thank American Chemet Corporation, USA, for providing the Cuprous Oxide samples used in this study.

8. Appendix A

Figure 8 provides surface topography maps for the eight test cuprous oxide specimens, a total of 32 surfaces from two applications and experiments. The maps are of 2 mm by 2 mm sections of the surface, and the vertical colour scale for surface elevation ranges from -60µm to 60µm for all the surfaces.

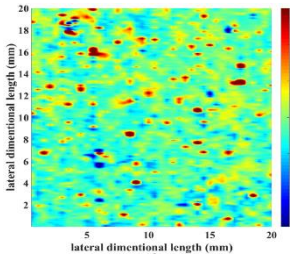

(***1***) Specimen C2 surface A of the 1st application

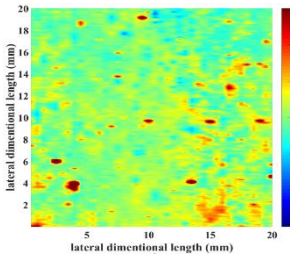

(***2***) Specimen C2 surface B of the 1st application

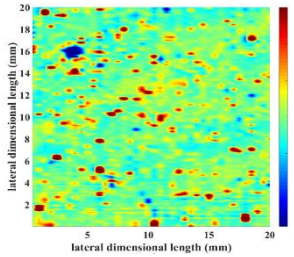

(***3***) Specimen C2 surface A of the 2nd application

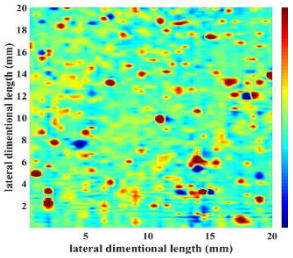

(***4***) Specimen C2 surface B of 2nd application

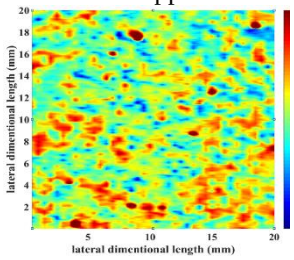

(***5***) Specimen C7 surface A of the 1st application

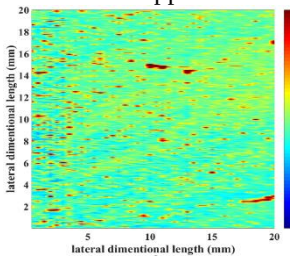

(***6***) Specimen C7 surface B of the 1st application

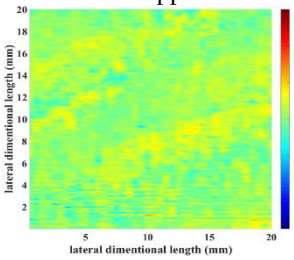

(***7***) Specimen C7 surface A of the 2nd application

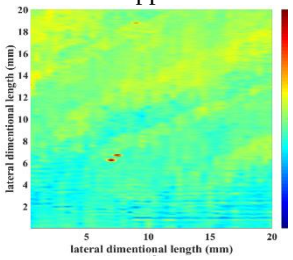

(***8***) Specimen C7 surface B of the 2nd application

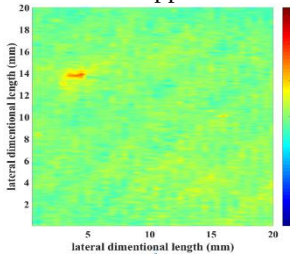

(***9***) Specimen C12 surface A of the 1st application

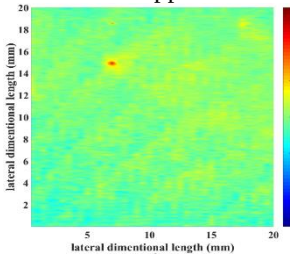

(***10***) Specimen C12 surface B of the 1st application

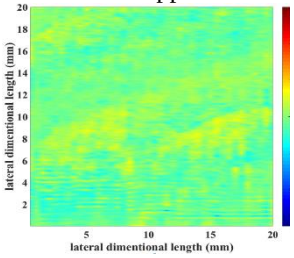

(***11***) Specimen C12 surface A of the 2nd application

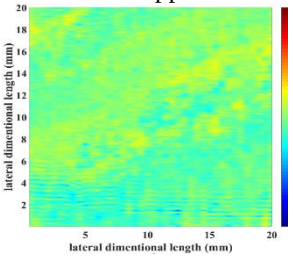

(***12***) Specimen C12 surface B of the 2nd application

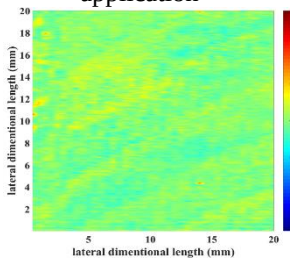

(***13***) Specimen C17 surface A of the 1st application

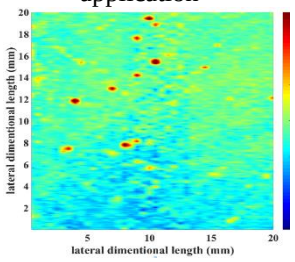

(***14***) Specimen C17 surface B of the 1st application

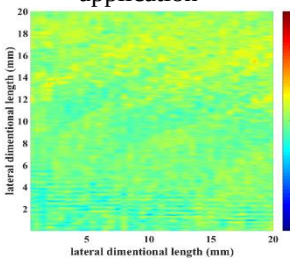

(***15***) Specimen C17 surface A of the 2nd application

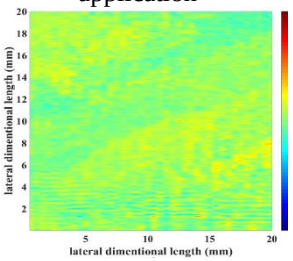

(***16***) Specimen C17 surface B of the 2nd application

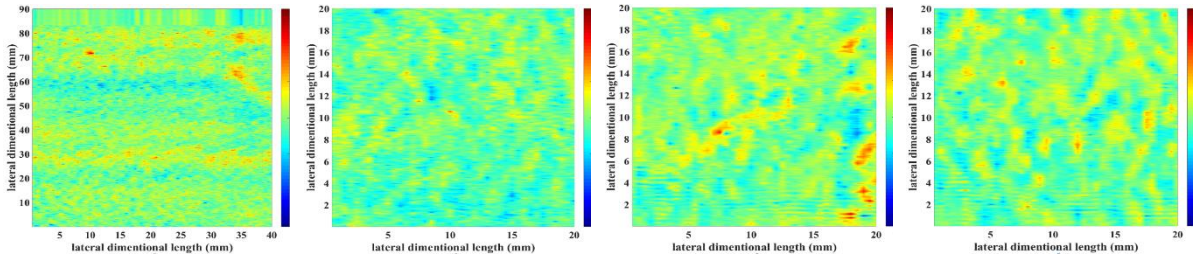

(***17***) Specimen C25 surface A of the 1st application

(***18***) Specimen C25 surface B of the 1st application

(***19***) Specimen C25 surface A of the 2nd application

(***20***) Specimen C25 surface B of the 2nd application

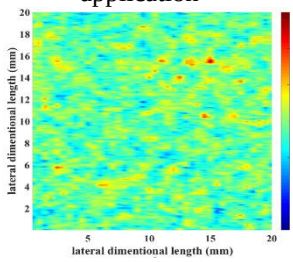

(***21***) Specimen C60 surface A of the 1st application

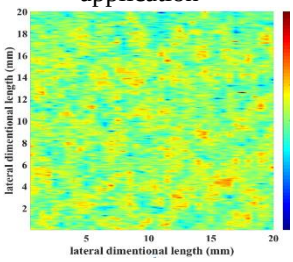

(***22***) Specimen C60 surface B of the 1st application

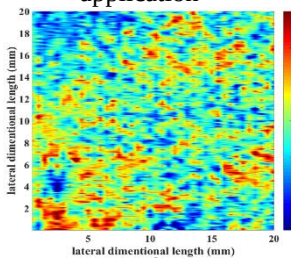

(***23***) Specimen C60 surface A of the 2nd application

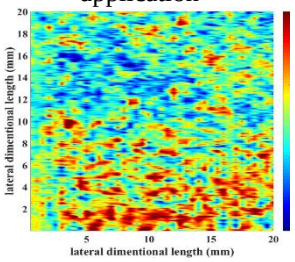

(***24***) Specimen C60 surface B of the 2nd application

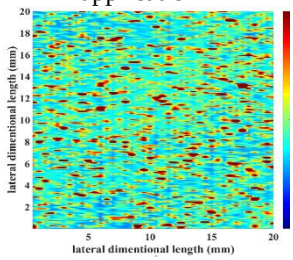

(***25***) Specimen C100 surface A of the 1st application

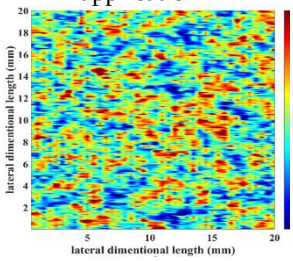

(***26***) Specimen C100 surface B of the 1st application

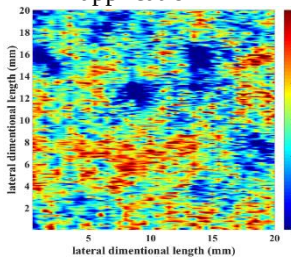

(***27***) Specimen C100 surface A of the 2nd application

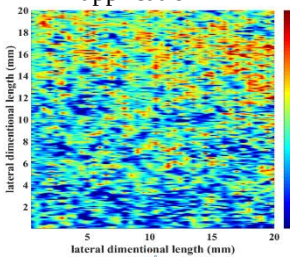

(***28***) Specimen C100 surface B of the 2nd application

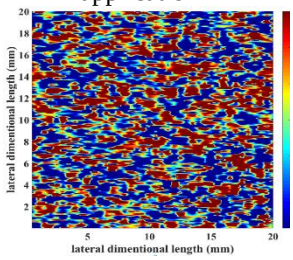

(***29***) Specimen C250 surface A of the 1st application

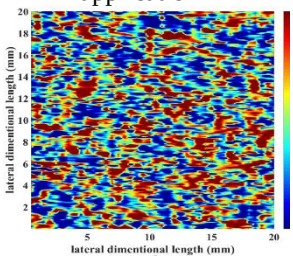

(***30***) Specimen C250 surface B of the 1st application

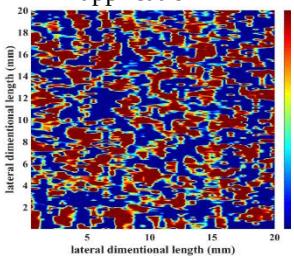

(***31***) Specimen C250 surface A of the 2nd application

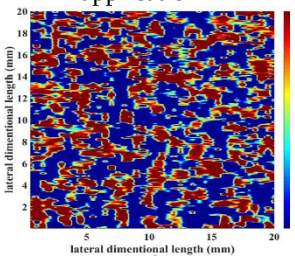

(***32***) Specimen C250 surface B of the 2nd application

Figure 8 (1−32): Topography maps of tested specimens

9. References:

Allen, J.J., Shockling, M.A. and Smits, A.J. (2005) 'Evaluation of a universal transitional resistance diagram for pipes with honed surfaces', Physics of Fluids, 17(12), p. 121702.

Aupoix, B. (2015) 'Roughness corrections for the k–ω shear stress transport model: status and proposals', Journal of Fluids Engineering, 137(2), p. 021202.

Bazin (1902) Expériences nouvelles sur la distribution des vitesses dans les tuyaux. Imprimerie nationale.

Candries, M. (2001) Drag, boundary-layer and roughness characteristics of marine surfaces coated with antifoulings. University of Newcastle upon Tyne Newcastle upon Tyne,, UK.

Candries, M. and Atlar, M. (2005) 'Experimental investigation of the turbulent boundary layer of surfaces coated with marine antifoulings', Journal of Fluids Engineering, 127(2), pp. 219-232.

Candries, M., Atlar, M. and Anderson, C.D. (2003a) 'Estimating the impact of new-generation antifoulings on ship performance: the presence of slime', Journal of Marine Engineering & Technology, 2(1), pp. 13-22.
Candries, M., Atlar, M., Mesbahi, E. and Pazouki, K. (2003b) 'The measurement of the drag characteristics of tin-free self-polishing co-polymers and fouling release coatings using a rotor apparatus', Biofouling, 19(S1), pp. 27-36.
Carlton, J.N. (1998) 'With cupric oxide surface coating, black pigments for antifouling paints used in marine environments'. Google Patents.
Clauser, F.H. (1954) 'Turbulent boundary layers in adverse pressure gradients', J. aeronaut. Sci, 21(2), pp. 91-108.
Colebrook, C.F., Blench, T., Chatley, H., Essex, E.H., Finniecome, J.R., Lacey, G., Williamson, J. and Macdonald, G.G. (1939) 'Correspondence. Turbulent flow in pipes, with particular reference to the transition region between the smooth and rough pipe laws. (Include plates)', Journal of the Institution of Civil engineers, 12(8), pp. 393-422.
Colebrook, C.F. and White, C.M. (1937) 'Experiments with fluid friction in roughened pipes', Proceedings of the royal society of london. series a, mathematical and Physical sciences, pp. 367-381.
Coleman, H.W. and Steele Jr, G. (1990) 'WG (1999). Experimentation and uncertainty analysis for engineers'. John Wiley and Sons, New York.
Darcy, H. (1857) Recherches expérimentales relatives au mouvement de l'eau dans les tuyaux. Mallet-Bachelier.
Dean, R.B. (1978) 'Reynolds number dependence of skin friction and other bulk flow variables in two-dimensional rectangular duct flow', Journal of Fluids Engineering, 100(2), pp. 215-223.
Durst, F., Fischer, M., Jovanović, J. and Kikura, H. (1998) 'Methods to set up and investigate low Reynolds number, fully developed turbulent plane channel flows', Journal of fluids engineering, 120(3), pp. 496-503.
Flack, K.A. and Schultz, M.P. (2010) 'Review of hydraulic roughness scales in the fully rough regime', Journal of Fluids Engineering, 132(4), p. 041203.
Granville, P.S. (1978) Similarity-law characterization methods for arbitrary hydrodynamic roughnesses. DTIC Document.
Granville, P.S. (1987) Proceedings of the Twenty-first American Towing Tank Conference. National Academies.
Hama, F.R. (1954) Boundary-layer characteristics for smooth and rough surfaces. SNAME.
Haslbeck, E.G. and Bohlander, G.S. (1992) Microbial biofilm effects on drag-lab and field. Naval Surface Warfare Centre Carderock DIV Annapolis MD.
Heslin, T., Heaney, J. and Harper, M. (1974) The effects of particle size on the optical properties and surface roughness of a glass-balloon-filled black paint. DTIC Document.
Holm, E., Schultz, M., Haslbeck, E., Talbott, W. and Field, A. (2004) 'Evaluation of hydrodynamic drag on experimental fouling-release surfaces, using rotating disks', Biofouling, 20(4-5), pp. 219-226.
Hopf, L. (1923) 'Die Messung der hydraulischen Rauhigkeit', ZAMM-Journal of Applied Mathematics and Mechanics/Zeitschrift für Angewandte Mathematik und Mechanik, 3(5), pp. 329-339.
Irzaman, I., Darmasetiawan, H., Hardhienata, H., Hikam, M., Arifin, P., Jusoh, S.N., Taking, S., Jamal, Z. and Idris, M.A. (2011) 'Surface roughness and grain size characterization of annealing temperature effect for growth gallium and tantalum doped Ba 0.5 Sr 0.5 TiO 3 thin film', Atom Indonesia, 35(1), pp. 57-67.
Kong, C.Y., Carroll, P.A., Brown, P. and Scudamore, R.J. (2007) 14th International Conference on Joining of Materials.
Ligrani, P.M. and Moffat, R.J. (1986) 'Structure of transitionally rough and fully rough turbulent boundary layers', Journal of Fluid Mechanics, 162, pp. 69-98.
Melo, L.L., Vaz, A.R., Salvadori, M.C. and Cattani, M. (2004) Journal of Metastable and Nanocrystalline Materials. Trans Tech Publ.
Moffat, R.J. (1988) 'Describing the uncertainties in experimental results', Experimental thermal and fluid science, 1(1), pp. 3-17.
Monty, J.P. (2005) Developments in smooth wall turbulent duct flows. University of Melbourne, Department of Mechanical and Manufacturing Engineering.
Moody, L.F. (1944) 'Friction factors for pipe flow', Trans. Asme, 66(8), pp. 671-684.
Nikuradse, J. (1933) VDI Forschungsheft. Citeseer.
Perron, A., Politano, O. and Vignal, V. (2008) 'Grain size, stress and surface roughness', Surface and Interface Analysis, 40(3-4), pp. 518-521.
Rawle, A. (2002) 'The importance of particle sizing to the coatings industry Part 1: Particle size measurement', Advances in Colour Science and Technology, 5(1), pp. 1-12.
Schiller, L. (1923) 'Über den strömungswiderstand von rohren verschiedenen querschnitts und rauhigkeitsgrades', ZAMM-Journal of Applied Mathematics and Mechanics/Zeitschrift für Angewandte Mathematik und Mechanik, 3(1), pp. 2-13.
Schultz, M.P. (2002) 'The relationship between frictional resistance and roughness for surfaces smoothed by sanding', Journal of fluids engineering, 124(2), pp. 492-499.
Schultz, M.P. (2004) 'Frictional resistance of antifouling coating systems', Transactions of the ASME-I-Journal of Fluids Engineering, 126(6), pp. 1039-1047.

Schultz, M.P. (2007) 'Effects of coating roughness and biofouling on ship resistance and powering', Biofouling, 23(5), pp. 331-341.
Schultz, M.P., Finlay, J.A., Callow, M.E. and Callow, J.A. (2000) 'A turbulent channel flow apparatus for the determination of the adhesion strength of microfouling organisms', Biofouling, 15(4), pp. 243-251.
Schultz, M.P. and Flack, K.A. (2007) 'The rough-wall turbulent boundary layer from the hydraulically smooth to the fully rough regime', Journal of Fluid Mechanics, 580, pp. 381-405.
Schultz, M.P. and Flack, K.A. (2009) 'Turbulent boundary layers on a systematically varied rough wall', Physics of Fluids, 21(1), p. 015104.
Schultz, M.P. and Flack, K.A. (2013) 'Reynolds-number scaling of turbulent channel flow', Physics of Fluids (1994-present), 25(2), p. 025104.
Smith, T.W.P., Jalkanen, J.P., Anderson, B.A., Corbett, J.J., Faber, J., Hanayama, S., O'Keeffe, E., Parker, S., Johansson, L. and Aldous, L. (2014) 'Third imo ghg study 2014', International Maritime Organization (IMO), London, http://www.iadc.org/wp-content/uploads/2014/02/MEPC-67-6-INF3-2014-Final-Report-complet.pdf.
Standard ISO 4287 (1997) 'Geometrical product specifications (GPS)–Surface texture: Profile method–Terms, definitions and surface texture parameters'.
Stanton, T.E. (1911) 'The mechanical viscosity of fluids', Proceedings of the Royal Society of London. Series A, Containing Papers of a Mathematical and Physical Character, 85(579), pp. 366-376.
Turkmen, S., Yeginbayeva, I. and Atlar, M. (2016) Evaluation of pressure drop methodology (SEAFRONT project Deliverable D4.19).
Ünal, B. (2012) Effect of surface roughness on the turbulent boundary layer. Istanbul technical university, graduate school of science engineering and technology.
Ünal, U.O. (2015) 'Correlation of frictional drag and roughness length scale for transitionally and fully rough turbulent boundary layers', Ocean Engineering, 107, pp. 283-298.
Ünal, U.O., Ünal, B. and Atlar, M. (2012) 'Turbulent boundary layer measurements over flat surfaces coated by nanostructured marine antifoulings', Experiments in fluids, 52(6), pp. 1431-1448.
von Mises, R. (1914) 'Elemente der technischen Hydrodynamik', Teubner, Leipzig.
Watanabe, S., Nagamatsu, N., Yokoo, K. and Kawakami, Y. (1969) 'The augmentation in frictional resistance due to slime', J. Kansai Society of Naval Architects, 131, pp. 45-51.
Xin, Z., Xiao-Hui, S. and Dian-Lin, Z. (2010) 'Thickness dependence of grain size and surface roughness for dc magnetron sputtered Au films', Chinese Physics B, 19(8), p. 086802.
Yeginbayeva, I. (2017) An investigation into hydrodynamic performance of marine coatings "in-service" conditions. Doctoral thesis. Newcastle University, United Kingdom.
Zanoun, E.-S., Nagib, H. and Durst, F. (2009) 'Refined cf relation for turbulent channels and consequences for high-Re experiments', Fluid dynamics research, 41(2), p. 021405.
Zhao, W. and Wang, X. (2015) 'Antifouling based on biocides: From toxic to green', in Antifouling Surfaces and Materials. Springer, pp. 105-134.